ELSEVIER

Contents lists available at ScienceDirect

# Earth and Planetary Science Letters

www.elsevier.com/locate/epsl



# From slab to surface: Earthquake evidence for fluid migration at Uturuncu volcano, Bolivia



Thomas S. Hudson<sup>a,\*</sup>, J-Michael Kendall<sup>a</sup>, Matthew E. Pritchard<sup>b</sup>, Jonathan D. Blundy<sup>a</sup>, Joachim H. Gottsmann<sup>c</sup>

- a Department of Earth Sciences, University of Oxford, UK
- b Department of Earth and Atmospheric Sciences, Cornell University, USA
- <sup>c</sup> School of Earth Sciences, University of Bristol, UK

#### ARTICLE INFO

# Article history: Received 29 March 2021 Received in revised form 22 October 2021 Accepted 25 October 2021 Available online 8 November 2021 Editor: H. Thybo

Keywords: volcano seismology arc volcanism tectonics magnitudes earthquakes

#### ABSTRACT

Uturuncu volcano is situated in the Bolivian Andes, directly above the world's largest crustal body of silicic partial melt, the Altiplano-Puna Magma Body (APMB). Uturuncu last erupted 250,000 years ago, yet is seismically active and lies at the centre of a 70 km diameter uplifted region. Here, we analyse seismicity from 2009 to 2012. Our earthquake locations, using a newly developed velocity model, delineate the top and bottom of the APMB, reveal individual faults, and reconcile differences in depth distribution between previous studies. Spatial clustering analysis of these earthquakes reveals the orientations of the faults, which match stress orientations from seismic anisotropy. Earthquake b-values derived from moment magnitudes (1.44  $\pm$  0.06) differ significantly from those using local magnitude measurements (0.80  $\pm$  0.03). From these observations and theoretical justification, we suggest that, if possible, moment magnitudes should be used for accurate b-value analysis. We interpret b-values > 1in terms of fluid-enhanced seismicity. Shallow seismicity local to Uturuncu yields b-values > 1.1 with some temporal variation, suggesting fluid migration along pre-existing faults in a shallow hydrothermal system, likely driven by advection from the APMB. Intriguingly, events deeper than the APMB also yield large b-values (1.4), mapping the ascent into the lower crust of fluids that we infer as originating from a subducting slab. Cumulatively, these results provide a picture of an active magmatic system, where fluids are exchanged across the more ductile APMB, feeding a shallow, fault-controlled hydrothermal system. Such pathways of fluid ascent may influence our understanding of arc volcanism, control future volcanic eruptions and promote the accumulation of shallow hydrothermal ore deposits.

© 2021 Published by Elsevier B.V.

# 1. Introduction

Uturuncu is a volcano in the Bolivian Andes. It sits above the Altiplano-Puna Magma (or Mush) Body (APMB), the world's largest zone of silicic partial melt (Pritchard et al., 2018). The extent of the APMB has been imaged by ambient noise tomography and receiver functions, suggesting a volume of 500,000 km³ of 20–30% partial melt at 15 to 20 km below sea-level (Chmielowski et al., 1999; Ward et al., 2013; Zandt et al., 2003). The APMB extent has also been constrained by magnetotellurics, gravity and petrological methods (Comeau et al., 2016; Schmitz et al., 1997). There is also evidence that melt may extend into the lower crust (Kukarina et al., 2017). Although Uturuncu last erupted 250,000 yrs ago (Muir et al., 2015), the volcano has been deforming for at least 50 yrs, at

a rate of up to 1 cm/yr between 1992 and 2004 (Gottsmann et al., 2018; Henderson and Pritchard, 2017; Pritchard et al., 2018), suggesting that the volcano might be a somewhat dynamic system.

A number of seismological and other geophysical studies have recently focussed on mapping the seismicity and imaging the crustal structure at Uturuncu. Both shallow and deep crustal seismicity, above and below the APMB, have been observed (Jay et al., 2012; Kukarina et al., 2017; Sparks et al., 2008). Moment tensor analysis of this seismicity has shown both double-couple (DC) shear earthquakes and earthquakes with a volumetric component (Alvizuri and Tape, 2016). Seismicity reveals a shallow stress field that mimics the orientations of the faults associated with these earthquakes (predominantly NE-SW and NW-SE) (Maher and Kendall, 2018). Analysis of local earthquake magnitudes suggests that *b*-values are significantly less than one (0.66) (Hutchinson, 2015; Jay et al., 2012; Maher and Kendall, 2018), in stark contrast to studies of volcanic regions elsewhere (Greenfield et al., 2020; Murru et al., 2007; Power et al., 1998; Wilks et al., 2017). The

<sup>\*</sup> Corresponding author.

E-mail address: thomas.hudson@earth.ox.ac.uk (T.S. Hudson).

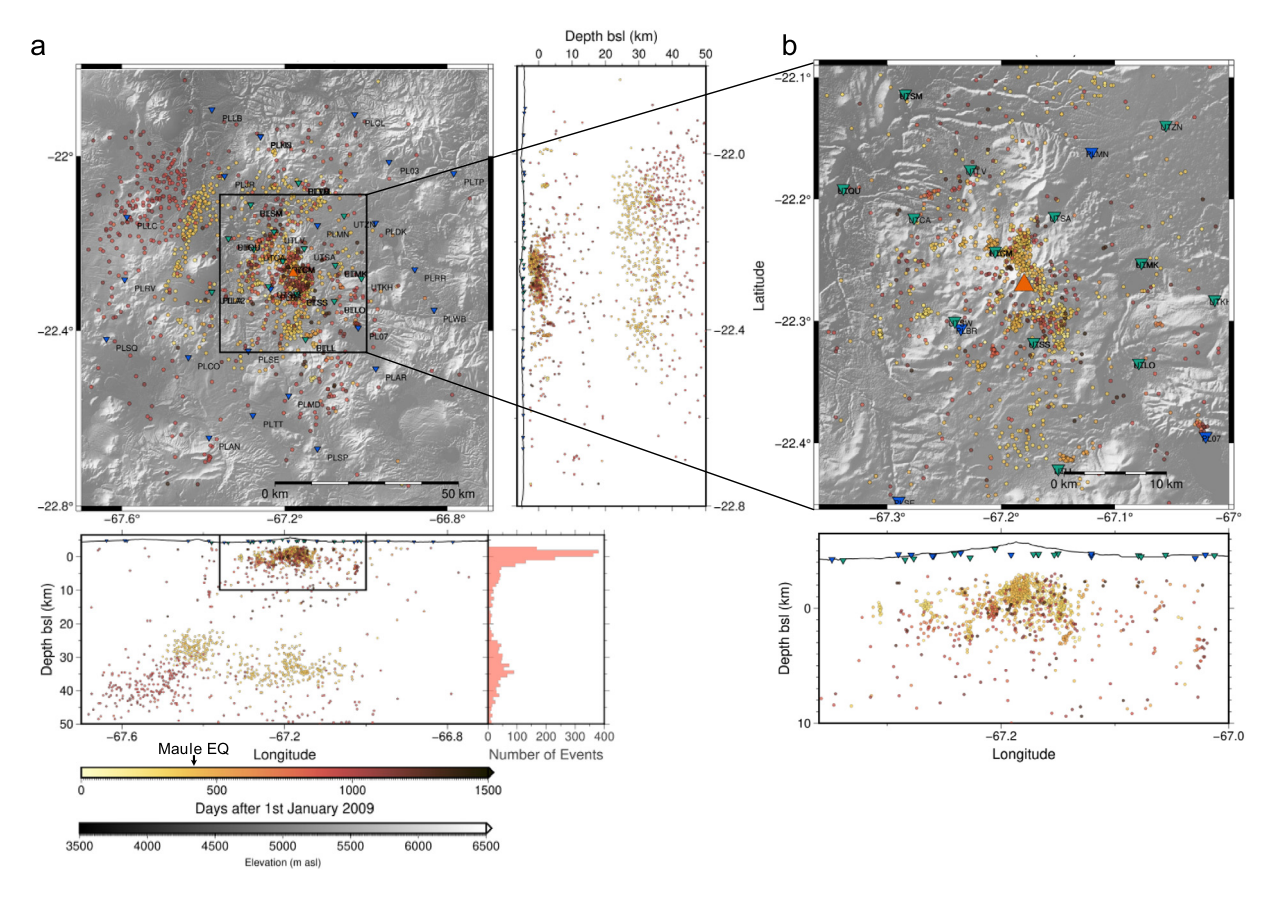


Fig. 1. Seismicity observed at Uturuncu between 2009 and 2012. a) Map of overall seismicity observed in the region surrounding Uturuncu, as well as latitude and longitude depth profiles. The summit of Uturuncu is shown by the orange triangle. Seismometers are shown by the green (ANDIVOLC) and blue (PLUTONS) inverted triangles. Depth profiles are taken through the summit of the volcano. Events are coloured by time. Note the significant rate of triggered seismicity due to the Maule earthquake, labelled on the time colour legend. b) Enlarged map and longitude depth profile of the seismicity in the immediate vicinity of Uturuncu. (For interpretation of the colours in the figure(s), the reader is referred to the web version of this article.)

seismic velocity structure of the crust has been constrained using receiver functions, body-wave tomography and ambient noise tomography (Chmielowski et al., 1999; Kukarina et al., 2017; Ward et al., 2014; Zandt et al., 2003). This seismic velocity structure, magnetotelluric (Comeau et al., 2016), and gravity (Del Potro et al., 2013) models image the APMB and a high conductivity, low density and slow shear-velocity region extending vertically from the APMB through the overlying upper crust.

Here, we use seismicity to address the question of how fluids migrate through the crust in an arc volcanic system and what role these fluids play in sustaining melt and hydrothermal systems at Uturuncu. We reanalyse seismic datasets recorded at Uturuncu between 2009 and 2010 and between 2010 and 2012, including a previously unstudied period in 2012. Previously, earthquakes were detected and located using travel-time picks at individual stations. Here, we use a method that combines energy from all stations simultaneously to improve the detection threshold, picking accuracy and provide error estimates (Hudson et al., 2019; Smith et al., 2020). This method allows us to detect more seismicity and map this seismicity and associated fault structures with higher accuracy than previous studies. Furthermore, we aim to address a depth discrepancy between previous studies (see Pritchard et al. (2018)). Earthquake moment magnitudes are calculated to assess b-values at various depths in the crust, with the aim of constrain the role and paths of fluid ascent through the crust at Uturuncu volcano. Any evidence of fluid migration above and/or below the APMB would aid our understanding of how the APMB and shallower hydrothermal systems are sustained at Uturuncu and arc volcanic systems more generally. To validate the use of moment magnitudes for *b*-values analysis, we revisit the debate associated with the use of local and moment magnitudes for calculating *b*-values. We present both observational and theoretical justifications for the use of moment magnitude for volcano-tectonic analyses, crucial for the understanding the role of fluids in volcanic systems from seismic observations.

# 2. Data and methods

Two seismometer networks were deployed over the period of 20<sup>th</sup> April 2009 to the 27<sup>th</sup> October 2012, with the ANDIVOLC network (Jay et al., 2012) (see gold inverted triangles, Fig. 1) operational until the 13<sup>th</sup> April 2010 and the PLUTONS network (Kukarina et al., 2017) (see blue inverted triangles, Fig. 1) operational for the remaining duration. The ANDIVOLC network comprised of nine Mark Products L22 2 Hz three-component seismometers and six Guralp CMG-40T 30 s three-component seismometers, all with Reftek RT130 dataloggers with a sampling rate of 50 Hz. The PLUTONS network comprised of thirty-three Guralp CMG-3T 120 s three-component seismometers, all with Reftek RT130 dataloggers with a sampling rate of 100 Hz.

# 2.1. Earthquake detection

These instruments were used to detect the seismicity in Fig. 1 using QuakeMigrate, a microseismic detection algorithm (Hudson et al., 2019; Smith et al., 2020). The QuakeMigrate method involves first band-pass filtering the data, before applying a Short-Term-Average (STA) to Long-Term-Average (LTA) algorithm to each

station and component individually. We use the Z component for P phases and the N and E components for S phases. These STA/LTA time series, henceforth referred to as onset functions, for each station are then combined. These signals are migrated through time and space to search for a coalescence of energy from the combination of peaks observed in the onset functions of individual stations. If the coalescence of energy at a particular point in 3D space at a given time is sufficiently high, then this triggers an event detection. The widths of the peaks in the onset functions are approximated to be Gaussian, as in Drew et al. (2013), which provides a measure of the temporal uncertainty associated with the P and S phase picks at individual stations. This quantification of phase pick temporal uncertainty is a key strength of the QuakeMigrate algorithm. We apply the OuakeMigrate algorithm to the Uturuncu seismic dataset to obtain an initial catalogue of earthquakes, with P and S picks and their associated uncertainties.

Once we have an initial catalogue, we relocate the events using the non-linear relocation algorithm NonLinLoc (Lomax and Virieux, 2000), in order to obtain robust hypocentral locations and uncertainties for the events. We then filter this catalogue by physically meaningful parameters, such as the depth uncertainty, in order to minimise the number of false detections in our catalogue. This also allows us to remove near-surface events likely of anthropogenic origin (for example, mining activity) that are located at shallow (<10 km bsl) depths, yet have anomalously high depth uncertainties compared to the depth uncertainties of other shallow earthquakes.

All parameters used in the QuakeMigrate earthquake detection and NonLinLoc relocation processes are given in Supplementary Table S1. The band-pass filter values used (2–20 Hz) mean that our catalogue is comprised primarily of volcano-tectonic seismicity rather than long-period and very-long-period seismicity. The velocity model used in the QuakeMigrate migration is a 1D approximation of the 3D velocity tomography results (see Supplementary Fig. S1).

# 2.2. Earthquake magnitudes

The magnitude of an earthquake defines the size or energy of an earthquake. Broadly there are two types of magnitude scale: relative magnitude scales, such as local magnitude,  $M_L$ ; and absolute magnitude scales, such as moment magnitude, Mw (Hanks and Kanamori, 1979). Although local magnitudes are easier to measure, absolute magnitudes provide an estimate of the actual moment or energy release of an earthquake rather than empirical measure. Moment magnitudes may therefore allow for more effective analysis of general trends in number of earthquakes vs. magnitude, as well as the underlying physical mechanisms generating the seismicity. We therefore use the moment magnitude scale, but also calculate local magnitudes for reference. Moment magnitudes are calculated using a Brune model fitted to the earthquake spectra (Brune, 1970; Stork et al., 2014). Local magnitudes are calculated from a newly-derived scale using the method of Illsley-Kemp et al. (2017). Descriptions of the exact methods used to calculate  $M_w$ and  $M_L$  in this study are provided in the Supplementary Material.

# 2.3. Calculation of overall and temporal variations in b-value

The Gutenberg-Richter distribution describes how usually there are many more smaller earthquakes than larger earthquakes, and this trend follows a logarithmic relationship described by,

$$\log_{10} N = a - bM,\tag{1}$$

where N is the number of earthquakes greater than a magnitude M, and a and b are constants describing the rate of seismic-

ity and the relationship between the rate of smaller and larger earthquakes, respectively. Globally, *b*-values are on average approximately 1.0 (El-Isa and Eaton, 2014). Perturbations in *b*-value are thought to be linked to prevailing effective stress conditions. Specifically, *b*-values greater than one are a result of processes that lower the effective stress on a fault such as an increase in pore pressure due to the presence of fluids at the fault (e.g. Schlaphorst et al. (2016)), thermal stress gradients (e.g. Warren and Latham (1970)), or material heterogeneities (e.g. Mogi (1962)), for example. High *b*-values could therefore indicate the possible presence of fluid migration.

To calculate overall earthquake catalogue *b*-values, we use the boundary-value-stability method of Roberts et al. (2015), with individual *b*-values calculated using the maximum likelihood method. Temporal variation in *b*-values is found using the method detailed in Roberts et al. (2016), which has proved successful for other volcano seismology studies (Greenfield et al., 2020). A full description of the methods used to calculate overall *b*-values and associated temporal variations are provided in the Supplementary Material.

# 2.4. Seismicity clustering analysis for delineating fault structure

Clustering analysis is performed on the shallower seismicity above the APMB and within 20 km of Uturuncu's summit. Our motivation for this is that this shallow seismicity might delineate shallow fault structures that would be otherwise challenging to observe. An approximation is made that if the seismicity in any given cluster is distributed along a single fault, then the principle component vector of the earthquake hypocentres within the cluster is assumed to represent the orientation of a linear fault.

The first step of the seismicity clustering and fault analysis method is to cluster the individual hypocentres into common clusters. There are many algorithms available to perform this clustering. The Density-Based Spatial Clustering for Applications with Noise (DBSCAN) algorithm of Ester et al. (1996) is applied to the data, as used in other seismicity clustering studies (for example, Cesca, 2020). This algorithm is appropriate for our spatial clustering problem since it is effective for 3D geometries with clusters of varying density and size. It also performs well compared to other methods for many samples with a number of clusters. The method groups together points that are densely distributed in space and separated by sparsely populated regions. Specifically the method comprises of the following steps:

- 1. First the algorithm selects a core sample. A core sample is defined as a sample that is surrounded by a minimum number of samples,  $n_{min}$ , within a maximum neighbourhood distance,  $d_{max}$ .
- 2. The algorithm then checks if each of the neighbouring points fulfil the aforementioned criteria to be a core sample. This process is repeated for all core samples to grow the cluster.
- 3. Steps (1) and (2) are repeated for randomly sampled points until all the data points are processed and either labelled in clusters, or as noise points that do not belong to a cluster.

The density of the clusters, and the algorithm performance, are therefore constrained by the parameters  $n_{min}$  and  $d_{max}$ . We set  $n_{min}$  to be 5.  $d_{max}$  is set to be 0.5 km, based on optimising the maximum number of clusters with the minimum number of unclustered earthquakes (see Supplementary Fig. S4).  $d_{max}$  is similar in magnitude to the typical earthquake depth uncertainty for these shallow earthquakes ( $\sim$ 0.5 km), but larger than the typical horizontal uncertainty ( $\sim$ 0.25 km).

Once the earthquakes are clustered, Principal Component Analysis (PCA) (Pearson, 1901) is used to find the vector that represents

the orientation of the cluster. If one assumes that the cluster represents seismicity along a fault, and that the fault is linear, then this vector represents the orientation of the fault. A summary of the PCA method applied to each cluster is as follows:

- The data is standardised by demeaning and dividing by the standard deviation.
- 2. The covariance of this standardised data is then calculated.
- 3. Finally, the eigenvalues and eigenvectors of the covariance matrix are calculated, with the eigenvector corresponding to the largest eigenvalue defining the principal component vector of the cluster, and therefore the fault orientation.

#### 3. Results

Fig. 1 shows the seismicity observed at Uturuncu from 2009 to 2012. The hypocentral depths of the shallow seismicity, less than 5 km bsl in Fig. 1b, are distributed with a mean depth of  $\sim$ 0 km bsl, resolving the depth discrepancy between earthquake depths in Jay et al. (2012) and Kukarina et al. (2017), which is shown explicitly in Pritchard et al. (2018). This shallow seismicity is generally located within 5 km laterally of the Uturuncu's summit. However, there are a number of distinct clusters of seismicity laterally offset by up to 20 km, approximately to the SE, S, W and NW. The majority of clusters of seismicity have approximately linear spatial distributions, oriented vertically or sub-vertically. There is no obvious temporal behaviour linking the individual clusters, aside from earthquakes thought to be triggered by the M8.8 Maule earthquake, Chile (Jay et al., 2012) (see Fig. 1), which occurred on 27<sup>th</sup> February 2010. However, although the activation of each cluster is apparently temporally random, each distinct spatial cluster is active only for a short period of time, of the order of 10s of days, before shutting off again.

We observe a gap in seismicity at depths between approximately 14 to 22 km bsl, see Fig. 1a, below which considerable activity at depths between 22 to 50 km bsl is observed. This deeper seismicity appears to show a distinct spatial-temporal trend, with the majority of deep seismicity directly under Uturuncu occurring in 2010, likely triggered by the Maule earthquake. Much of the deeper seismicity to the NW occurs later. While there could be a physical cause of this observation for the seismicity directly under Uturuncu, the spatial-temporal trend of seismicity offset to the NW is likely a result of the ANDIVOLC network aperture not being sufficiently large to provide adequate earthquake detection and hypocentral constraint in this region compared to the PLUTONS network, which has a wider aperture.

Fig. 2 shows examples of the displacement spectra and associated Brune model fits used to calculate the moment magnitudes for two earthquakes, of magnitudes 2.8 and 1.5. These events exemplify the spectra of the largest and smallest events detected. The observed spectra for each event are similar for each of the four stations shown in Fig. 2a-d. The blue and red solid lines show the noise-removed observed spectra for the large and small event, respectively, with the spectra prior to noise removal shown by the grey lines. For the larger event, the signal dominates over the noise at lower frequencies, with the noise having a negligible effect on the long-period spectral level and hence the moment magnitude. The same statement is also generally valid for the smaller event at most stations, although in this case, the signal at station PLRR, Fig. 2c, is clearly affected by the noise. The corner frequencies for the smaller event are likely underestimated due to the loss of high frequency signals below the noise (Butcher et al., 2020). However, with the noise removed, the Brune model fit, shown by the dashed lines in Fig. 2, provides a good fit for the longperiod spectral level (the amplitude at near-zero frequency) for all the observed earthquake spectra. Although the corner frequen-

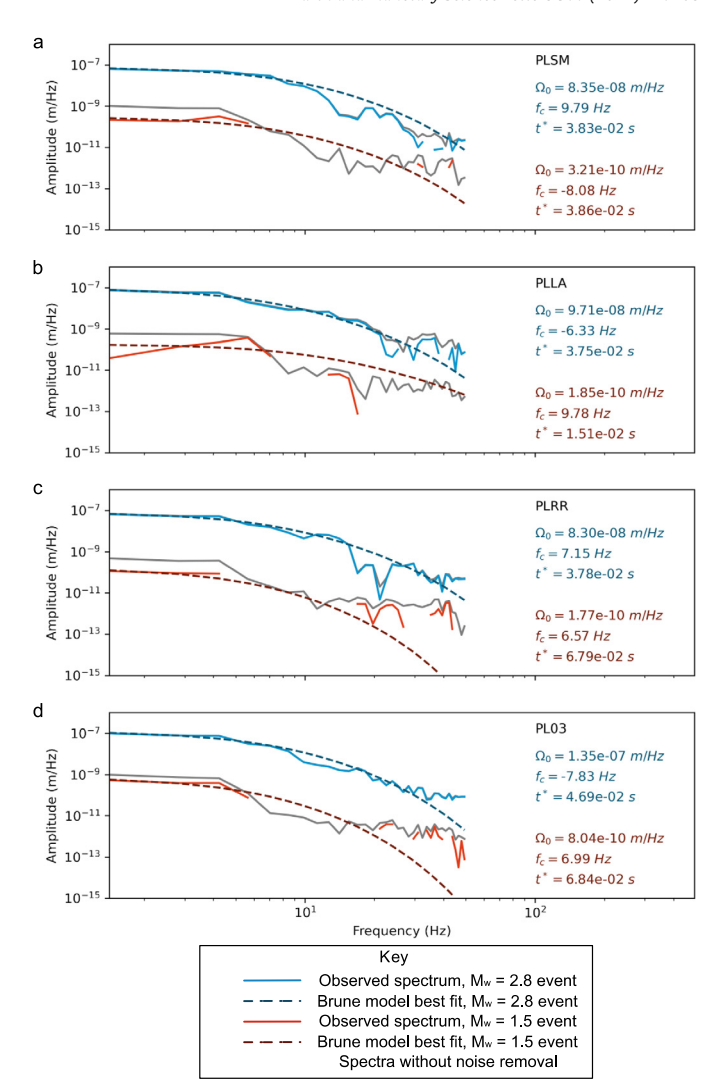


**Fig. 2.** Examples of earthquake source displacement spectra for two events at four stations: PLSM, PLLA, PLRR and PLO3, labelled (a) to (d), respectively. Both events are located in the immediate vicinity of Uturuncu, as defined by Fig. 1b. The first event is a  $M_w = 2.8$  event, shown in blue, and the second event is a  $M_w = 1.5$  event, shown in red. The solid lines show the observed spectra and the dashed lines show the best fitting Brune model. The grey lines show the spectra prior to noise removal.

cies of the Brune model fits are in some cases poorly resolved, since it is only the observed long-period spectral level that is used to calculate  $M_w$ , we are therefore confident that we can accurately measure  $M_w$  over the magnitude range observed in this study.

The moment magnitude earthquake cumulative frequency distribution for the entire Uturuncu seismicity catalogue is shown by the black points in Fig. 3. The green points show the values of the individual bins for the moment magnitude data. The relatively broad turning point in these binned events compared to some other volcanic-seismicity datasets (e.g. Greenfield et al. (2018)) is likely a combination of a varying network geometry, varying noise conditions and the bimodal depths of seismicity, caused by the APMB. The best fitting Gutenberg-Richter relationship for  $M_w$  is indicated by the blue line. The best fitting parameters are found using the BVS method (Roberts et al., 2015), with a magnitude of completeness of 2.28 and a b-value of 1.44  $\pm$  0.06 for 2,363 earthquakes. Similar analysis for the individual ANDIVOLC and PLUTONS networks, as well as the data excluding earthquakes triggered by the 2010 Maule, Chile, earthquake, gives similar b-values, all

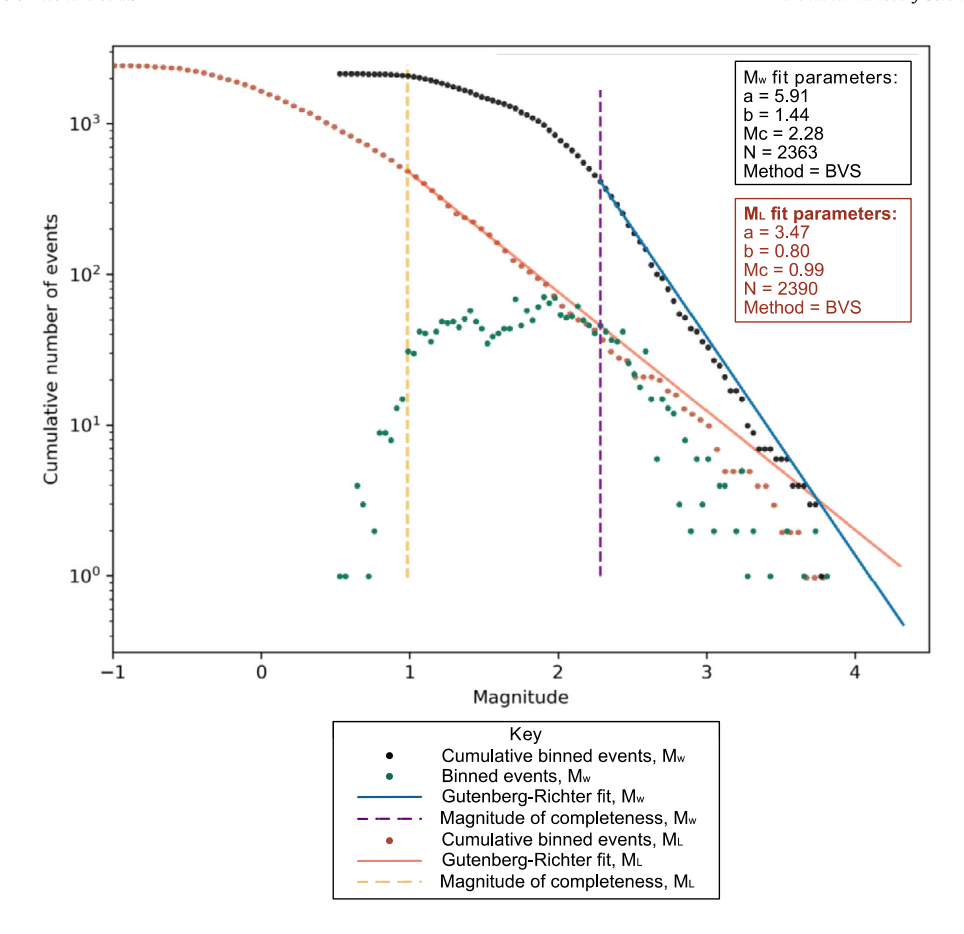


**Fig. 3.** Gutenberg-Richter plot of cumulative number of events vs. magnitude. The moment magnitude,  $M_{\rm w}$ , catalogue is plotted in black. The local magnitude catalogue is plotted for comparison in red. Magnitudes of completeness for the respective catalogues are shown by the dashed lines. Parameters labelled in the figure are as follows:  $M_{\rm w}$  is moment magnitude;  $M_{\rm L}$  is local magnitude; a is the number of M=0 earthquakes that would be observed if all earthquakes were observed for a given fit; b is the b-value of the given fit;  $M_{\rm C}$  is the magnitude of completeness associated with a given fit; and N is the number of earthquakes in the catalogue used for the various magnitude analyses. Additionally, BVS stands fo ther b-value stability method.

greater than one (see Supplementary Fig. S2). Local magnitudes for the Uturuncu seismicity catalogue give a b-value of  $0.80\pm0.03$  for a magnitude of completeness of 0.99 using the BVS method with the same parameters. Our b-value < 1.0 from local magnitudes is consistent with the values of 0.49 and 0.66 found using local magnitudes in other studies at Uturuncu (Jay et al., 2012; Maher and Kendall, 2018). The discrepancy between our result and theirs is a result of their use of a California  $M_L$  scale whereas we derive our own scale for the Uturuncu region specifically. This  $M_L$  b-value of 0.80 is in stark contrast with the b-value of 1.44 derived from moment magnitudes.

Temporal variation in earthquake moment magnitudes and bvalues of sub-regions of the study area are also investigated. Temporal variation of moment release and b-values are shown in Fig. 4. The two regions are defined in Fig. 4a. Fig. 4b shows the number of events per day and the cumulative moment release through time. The triggered events on the 27th February 2010 from the Maule earthquake can be clearly seen, with significant moment release occurring over a duration of only a few days. The shallow system, Region 1, appears to have an otherwise relatively stable release of seismic energy through time. However, the deeper seismicity in Region 2 releases seismic energy sporadically, releasing significantly more seismic energy in mid 2011 than early 2011, before tailing off again later that year. Fig. 4c shows the magnitude of completeness of the catalogue through time compared to the typical noise level during the observation period. M<sub>noise</sub> is defined here as the moment magnitude of a hypothetical earthquake with long-period spectral level equal to the seismogram noise level at a

distance of 30 km from a receiver. Obviously the assumed distance affects the result, but not by more than one order of magnitude for our range of possible hypocentral distances. Although there are several periods of higher noise levels, the noise is typically significantly below the magnitude of completeness level throughout the study period. Fig. 4c and Fig. 4d show the temporal variation in b-value for Regions 1 and 2, respectively. The gold line shows when the network transitioned from the ANDIVOLC to the PLUTONS network. The lower b-values observed by the ANDIVOLC network before 2010 are thought to be network effects, affecting the overall magnitude of completeness and so shouldn't be interpreted in any detail. Although the dataset does have a sufficient number of events to perform temporal b-value analysis, it is likely at the lower limit, and so short period temporal variations should be treated cautiously. However, we can confirm that both Regions 1 and 2 have b-values greater than one for the majority of the study period, with average b-values of 1.12 and 1.41, respectively. This is in contrast to previous studies (Jay et al., 2012; Maher and

A final analysis is to interrogate any spatial clustering present in the shallow seismicity observed in Region 1 of Fig. 4. The motivation for this is to delineate any fault structures and compare fault orientations to the prevailing stress regime and observed seismic anisotropy at Uturuncu. The shallow seismicity clustering and fault orientation results are shown in Fig. 5. The DBSCAN method clusters the data into 28 clusters, as shown by the different coloured scatter points in Fig. 5a,b. While the majority of earthquakes are clustered, there a small number of events that visually appear to

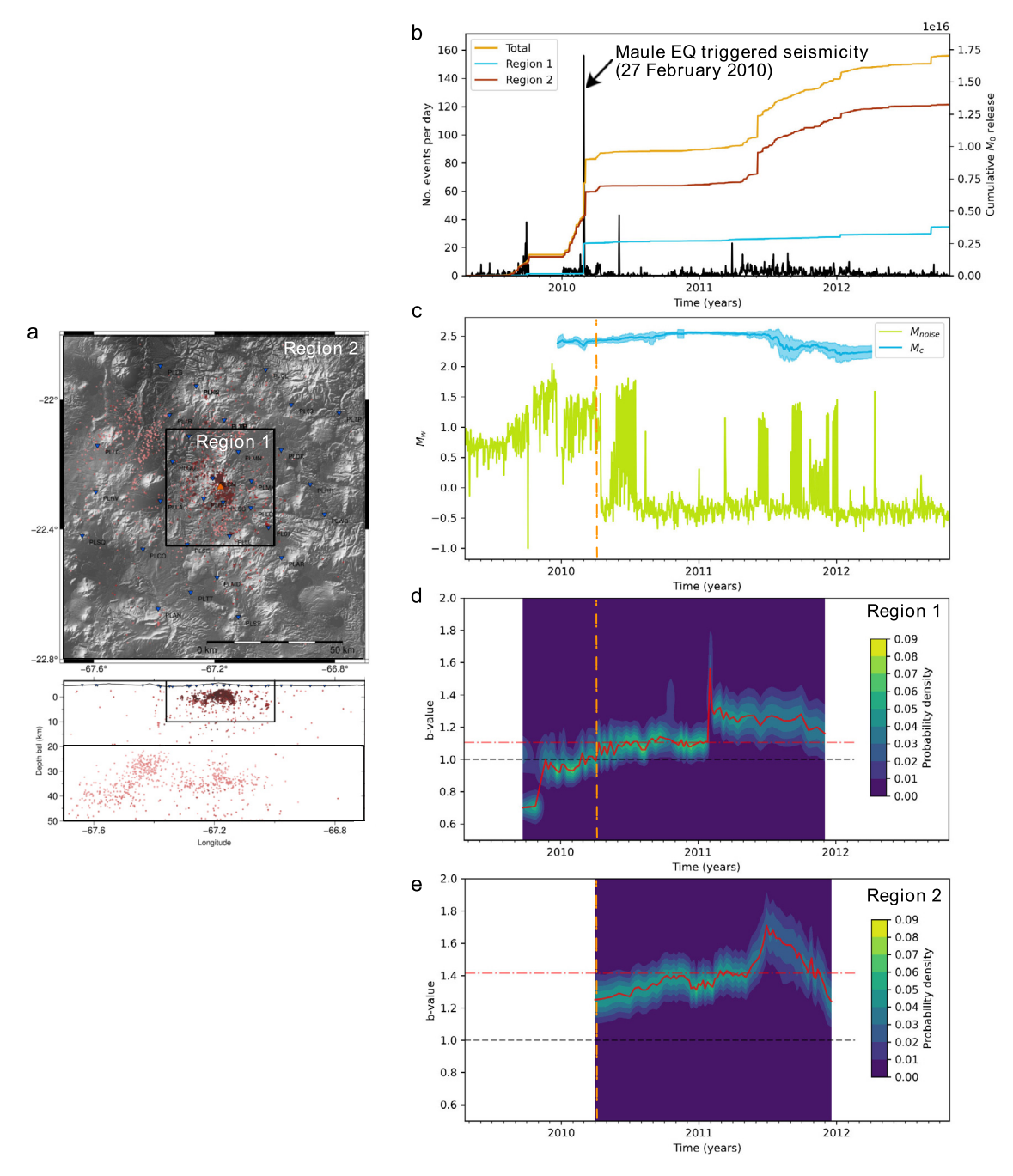


**Fig. 4.** Temporal variation in earthquake magnitudes and b-values. a) Map and depth profile defining the two regions used in (b), (d) and (e). b) Plot of number of events per day and cumulative moment release per day through time. c) Plot of magnitude of completeness through time compared to the representative daily noise level. The noise level is measured at 12:01 UTC each day, for an assumed epicentral distance of 30 km and an isotropic radiation pattern. d) Plot of b-value through time for region 1, using the method described in Roberts et al. (2016). e) Same as (d), but for region 2. 5000 random windows of sizes 50 to 500 are used to obtain the temporal b-value variation. We stack every 10 samples to smooth the PDFs. The black line indicates b = 1. The orange line indicates when the seismic network transitioned from the ANDIVOLC network to the PLUTONS network.

be clusters but are not clustered in our analysis. However, we prefer an automated clustering algorithm over manual inclusion of all events because it is unbiased, with a clear theoretical basis. There is therefore greater confidence in the results for earthquakes that do cluster, while still providing with an overall picture of possible faults delineated by this seismicity. It is also worth noting that one cluster of events centred at  $\sim 2.5$  km directly north of the Uturuncu summit (see Fig. 5a) is comprised of hundreds of events. Fig. 5a,b also show the fault PCA vectors in gold. These fault orientations indicate that the PCA method provides a useful method of determining the orientation of the clusters in three-

dimensions. Here, the assumption is made that these PCA vectors represent linear-approximated fault orientations. Fig. 5c shows the fault strikes for these PCA vector orientations. The Rose diagram shows the number of faults in 10° bins. There are predominantly two fault directions: the first NE-SW; and the second approximately perpendicular, with a NW-SE strike. This is in broad agreement with the anisotropy results of Maher and Kendall (2018), shown by the red bins in Fig. 5c. Fault dips are also shown relative to vertical. The fault dips are observed to be almost all far from vertical, with a dominant orientation of 50° to 60° from vertical (see Fig. 5d).

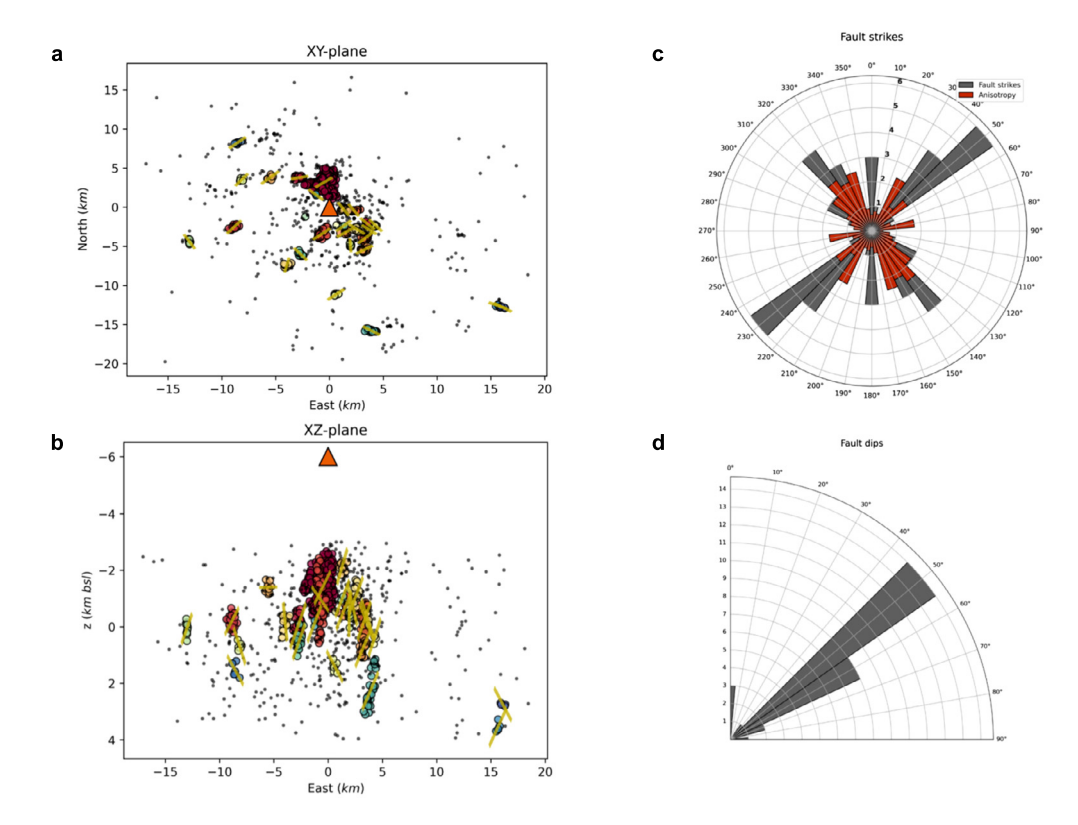


Fig. 5. Shallow seismicity fault cluster analysis. a) Map of horizontal spatial distribution of seismicity, coloured by cluster (28 clusters in total). Principal axes of the clusters plotted by gold lines from PCA analysis. Orange triangle shows the location of the summit of Uturuncu. b) Same as (a) but for an East-West depth profile. c) Rose diagram showing the orientation of the principal component vectors' strikes in black. Red data show the anisotropy results of Maher and Kendall (2018) for comparison. d) Rose diagram showing the dips of the faults from vertical (up is positive). Note that the anisotropy data plotted in (c) is scaled simply to provide a comparison of orientation rather than magnitude of anisotropy.

# 4. Discussion

We first emphasise the importance of, and justification for, using the moment magnitude scale for the calculation of b-values. These b-values are fundamental for the interpretation of the entirety of our later discussion of fluids in arc volcanic systems. After justifying our confidence in our b-value observations, we then discuss the interpretations and implications of our results for Uturuncu and other arc volcanic systems.

### 4.1. The importance of magnitude scale for b-values

Our results clearly show the difference in b-value measurements using local vs. moment magnitude scales. B-values > 1 are found when using moment magnitudes, compared to values < 1 observed using local magnitudes. This difference in b-value is significant, as it suggests a completely different crustal stress regime. With a b-value > 1 suggesting lower than expected normal stresses on the faults, resulting in more smaller magnitude earthquakes than for tectonic seismicity, in contrast to a b-value < 1 corresponding to higher than expected normal stresses. This discrepancy has significant implications for the identification of the causative processes of such seismicity, as evidenced later in this study. The question this disagreement raises is: which measure provides an accurate, valid measure of b-value?

We suggest that moment magnitude is the appropriate measure to use for b-value analyses, and that local magnitude derived b-values should be treated with caution. The most compelling justification for this is the theoretical basis for a break in the scaling factor of  $M_L$  and  $M_w$  for smaller earthquakes compared to larger earthquakes (from  $M_L \propto M_w$  to  $M_L \propto 1.5~M_w$ , for  $M_w < 1.5~M_w$ ), for  $M_w < 1.5~M_w$ 

2-3) (Deichmann, 2017) (also see Supplementary Fig. 3b). Deichmann (2017) describes this theoretical basis, verified with observations, to show that intrinsic scaling properties of the moment-rate function and attenuation characteristics of the medium cause the higher frequency energy of smaller earthquakes observed at a receiver to be more highly attenuated relative to the energy observed from large earthquakes. This effect manifests itself in the  $M_L$  scale since  $M_L$  uses the maximum amplitude of a seismic phase in the time-domain, which can be affected by a loss of high frequency energy. In contrast,  $M_w$  uses the long-period spectral level, which is approximately isolated from this effect until the energy is extremely highly attenuated. This is likely the behaviour observed here, as is observed in other data (Butcher et al., 2020), and is why an absolute measure of moment such as  $M_w$  should be used over  $M_L$  if possible in all instances, but especially in highly attenuating regions with low magnitude earthquakes ( $M_W < 2-3$ ), such as at volcanoes.

Our results provide further evidence that  $M_w$  should be used instead of  $M_L$  for b-value analyses, with our b-value calculations effected by the aforementioned magnitude scaling relationship. The moment magnitude is a physically meaningful measure, which does not rely upon empirically derived correction terms that can vary by orders of magnitude. In our case the moment magnitudes are in close agreement with those calculated from full waveform inversions of the same seismicity (Alvizuri and Tape, 2016) (see Supplementary Fig. S3). A further indication that moment magnitude is that a more accurate, valid measure of b-value here is that it provides a b-value greater than one, which is expected for volcanic systems with fluids present (Schlaphorst et al., 2016). Although b-values less than one have been observed for the crust in the vicinity of volcanoes, regions of fluid or partial melt at these volcanoes are found to have b-values greater than one (Farrell et

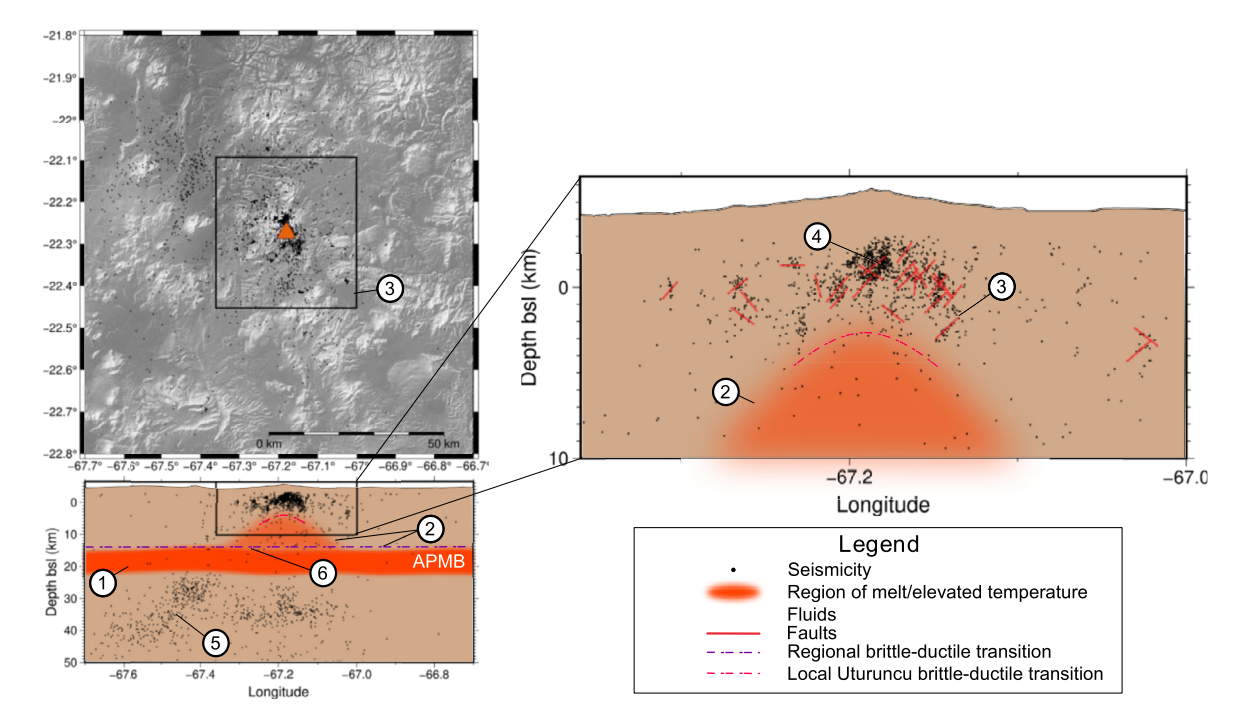


Fig. 6. Schematic summary of the interpretations from the seismicity results presented in this study. Black dots are observed seismicity. Numbered points are referred to in the text.

al., 2009; Greenfield et al., 2020; Murru et al., 2007; Power et al., 1998; Wiemer et al., 1998; Wilks et al., 2017).

# 4.2. New insights of Uturuncu

Fig. 6 summarises the seismic observations and the key interpretations of this study, (1) to (6), which provide new insights into Uturuncu and the underlying crust. There are six main conclusions from our findings, which help explain other geophysical and geochemical observations (see Fig. 7) and provide insights regarding the flow of fluids through the crust. These findings are described below, with an explanation of how they fit with other studies of Uturuncu.

(1) An absence of seismicity between  $\sim$ 14 to 22 km bsl (see Fig. 1) delineates the top and bottom of the ductile, elevated temperature signature of the APMB. The deeper bound of this region was not observed clearly in previous studies (Jay et al., 2012; Kukarina et al., 2017) due to a lack of detected earthquakes and low confidence in the locations of events that were detected. This absence of seismicity is likely a result of the crust within the vicinity of the APMB being too hot and therefore too ductile to sustain the release of seismic energy via brittle failure. The top of the APMB (see Fig. 6), constrained by the absence of seismicity, is in agreement with imaging of the APMB from ambient noise tomography, receiver functions, and magnetotellurics (see Fig. 7) (Chmielowski et al., 1999; Comeau et al., 2016; Pritchard et al., 2018; Ward et al., 2014). Our observations also provide new constraint on the bottom of the APMB, with seismicity observed at depths of greater than 22 km bsl, below the APMB.

The presence of a seismogenic zone beneath the APMB is an interesting result, since it provides evidence for either a brittle, elastic crust rather than a melt-rich crust extending towards the mantle, or the presence of fluids within critically stressed faults (Greenfield and White, 2015; T. S. Hudson et al., 2017). Although the temperature profile for the crust is not explicitly known at Uturuncu, the crust below the APMB is likely below the brittle-ductile transition. However, the lack of temporal migration of this seismicity, combined with the diffuse spatial, sub-horizontal vari-

ation correlating with apparent fault structures suggests that any melt migration would be highly sporadic, and some of this seismicity is likely triggered somehow by stress changes in the crust as a result of the M8 Maule earthquake. Moment tensor inversions might provide additional confirmation of this interpretation, although we do not pursue this here. Our favoured interpretation based on the limited observations is that this seismicity is likely associated with ascent of fluids along critically-stressed, fluid-rich faults in a possibly ductile crust. Evidence that the faults are critically-stressed is provided by the significant additional seismicity triggered by stress perturbations due to the M8.8 Maule earthquake. Evidence for fluid-rich faults is based upon high *b*-values, as discussed in interpretation point (5), later in this text.

(2) The spatial distribution of seismicity suggests that the regional seismic brittle-ductile transition zone is located at  $\sim$ 14 km bsl (purple dashed line, Fig. 6), with a local increase in the elevation of the brittle-ductile transition to  $\sim$ 4 km bsl (pink dashed line, Fig. 6), approximately beneath Uturuncu's edifice. This local brittle-ductile transition zone depth is consistent with the findings of Jay et al. (2012). The depth of the brittle-ductile transition zone is governed by crustal rheology, which itself is likely controlled by temperature. The  $\sim$ 14 km bsl depth of the regional brittle-ductile transition here is assumed to define the upper possible extent of the elevated temperature APMB. Likewise, an increase in elevation of the brittle-ductile transition to ~4 km bsl local to Uturuncu is likely caused by elevated temperatures due to the presence of melt pockets, or perhaps hot saline fluids, connecting the APMB to the shallower volcano. Approximate constraint for the depth of this brittle-ductile transition zone is provided by clusters of seismicity, such as those laterally offset from the summit of Uturuncu at longitudes of 67.23° N and 67.14° N. However, we cannot confidently make further inferences on the topography of the brittle-ductile transition without longer duration sampling of the seismicity. A shallow ductile region with elevated crustal temperatures local to Uturuncu is consistent with a higher conductivity region observed by magnetotelluric imaging (Comeau et al., 2016), a low density region ( $-150 \text{ kg m}^{-3}$  density contrast) from gravity data extending from the APMB to approximately sea-level (Del Potro et al., 2013),

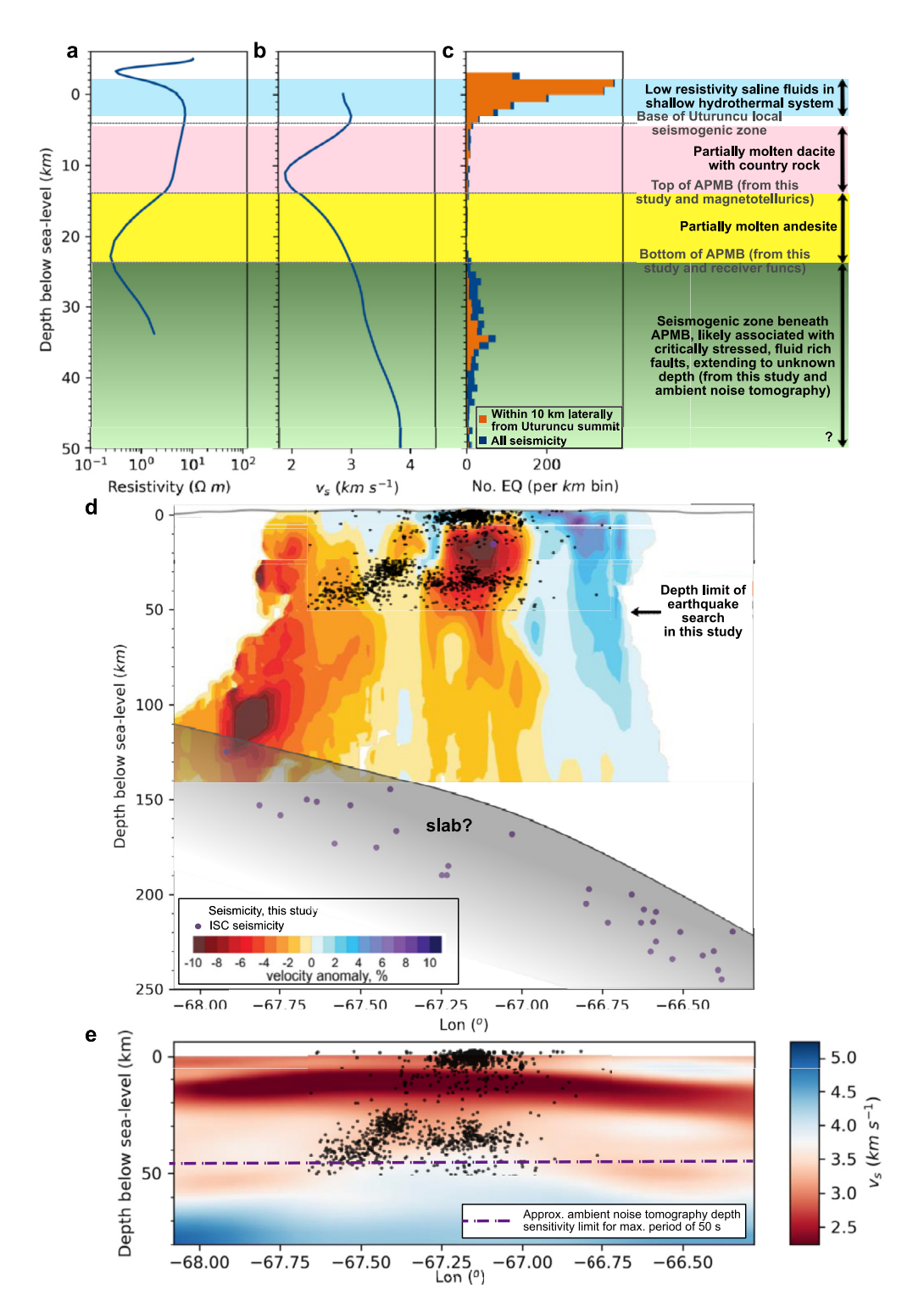


Fig. 7. Summary of how the results of this study compare with observations from previous studies. (a)–(c) Depth profiles of resistivity (Comeau et al., 2016),  $v_s$  from ambient noise tomography (Ward et al., 2013), and seismicity binned by depth (from this study). Interpretations shown are based on those presented in Pritchard et al. (2018) (Fig. 2) and references therein, along with the new contributions from this study. (d) Plot of S-wave tomography results of Kukarina et al. (2017), overlaid with the seismicity from this study (black scatter points), as well as International Seismological Centre (ISC) earthquakes (purple scatter points). Note that we only present seismicity detected up to 50 km bsl in this study (search grid ends at 50 km bsl). Note that the slab region is a rough guess, based on the results of Cahill and Isacks (1992), Prezzi et al. (2009), Kukarina et al. (2017) and ISC data. (e) Joint ambient noise tomography and receiver function inversion results of Ward et al. (2017), overlaid with the seismicity from this study. The colournap is referenced to the average  $v_s$  for the entire data volume. The purple dashed line indicates the approximate limit of sensitivity of the ambient noise tomography in this study.

and the centre of a 70 km diameter area of uplift (Gottsmann et al., 2018). Del Potro et al. (2013) suggest up to 25% partial melt within the low density body ascending diapirically rather than via diking. There is no evidence for active diking at present, as shown by the near-total absence of seismicity at that depth (Rubin, 1993). However, our observation period is of insufficient duration to interrogate seismic vs. aseismic migration of melt at this volcano. The observed uplift deformation has been investigated using geophysical and petrological observations, combined with thermomechanical modelling (Gottsmann et al., 2017). This modelling suggests that the uplift could be caused by either: an igneous mush column extending from the APMB to 6 km bsl; or a hybrid column composed of an igneous mush below a solidified and permeable body extending from the APMB to around sea-level. Our observations cannot prove or disprove either hypothesis.

(3) Shallow seismicity delineates fault structures, indicated by the red solid lines in Fig. 6, derived from the seismicity clustering analysis presented in Fig. 5. These clusters of seismicity switch on and off randomly, with each cluster only active for an order of days to tens of days at a time (see Fig. 1). These clusters are approximately linear in geometry, verifying that our linear-fault approximation is valid. The close agreement between the two families of fault strikes and a previous study of anisotropy (Maher and Kendall, 2018) suggests that observed anisotropy is primarily controlled by the faulting and/or orientations of the stress regime. We cannot rule out faults with other orientations present at Uturuncu, but can say that any such faults are not seismically active during the observation period, and so if they do exist then they are likely locked by the crustal stress regime. Another interesting observation is that the fault dips are not vertical or sub-vertical (see Fig. 5d), as observed at other volcanoes (Greenfield and White, 2015; Hudson et al., 2017; Lavayssière et al., 2019; Shelly and Hill, 2011). This observation provides further evidence that the faulting is likely controlled by the long wavelength stress regime driven by regional deformation, such as the 150 km diameter deformation anomaly observed by InSAR, GNSS and levelling (Gottsmann et al., 2018). Furthermore, there is no observed systematic variation in the vertical orientation of these faults focussed directly towards Uturuncu's summit that would be associated with ring-faulting centred about a shallow deformation signal. Overall, the earthquake clustering and PCA vector analysis shows that the seismicity clearly delineates fault structures, oriented so as to accommodate perturbations in the crustal stress regime.

(4) High b-values (>1) of the shallow seismicity in Region 1, local to Uturuncu, are most likely associated with a reduction in the effective normal stress of the faults imaged in (3). El-Isa and Eaton (2014) provide a comprehensive discussion of the mechanisms that reduce the effective normal stress of a fault, and hence cause elevated b-values. Here, we discuss some of the most plausible mechanisms at Uturuncu. Such high b-values are observed at other volcanoes (Bridges and Gao, 2006; Greenfield et al., 2018; Roberts et al., 2015). One possible cause of high b-values could be inflation reducing the normal stress on the faults (Bridges and Gao, 2006). However, the general lack of any spatial-temporal correlation in activity and apparent lack of interaction between the clusters of seismicity discussed in (3) implies that the seismicity is not modulated primarily by the crustal stress state, but by something in the immediate vicinity of the individual faults. Thermal stress gradients could also cause higher b-values (Warren and Latham, 1970), but this is thought unlikely as the shallow system is thought to be hydrothermal rather than magmatic, with correspondingly lower temperature gradients. In any case, any thermal gradients would require the advection of heat via fluids, which would likely travel along fault structures. We suggest that the reduced normal stresses on the faults are caused by elevated pore pressures due to the trapping and/or migration of fluids within

the fault systems (Schlaphorst et al., 2016). This interpretation is consistent with the interpretations from seismic anisotropy studies, suggesting fluids within the faults (Leidig and Zandt, 2003; Zandt et al., 2003), and moment tensor analysis that suggests that the shallow (<4 km bsl) seismicity within the immediate vicinity of the volcano exhibits predominantly opening tensile cracks and opening cracks with an explosive component (Alvizuri and Tape, 2016). Furthermore, this interpretation might also explain the high electrical conductivity anomaly at shallow depths from magnetotelluric measurements (Comeau et al., 2016).

Assuming that fluids do play a role in the shallow seismicity observed at Uturuncu, it encourages the question: are the fluids melt, or water and/or other volatiles. It is suggested that the shallow seismicity is associated with a hydrothermal system rather than melt for the following reason. It is difficult to conceive of significant partial melt volumes this shallow in the crust, without there being a surface expression of such melt. There is no evidence for eruptive activity at Uturuncu in the last 250,000 yrs (Pritchard et al., 2018). It is therefore assumed that the shallow system is hydrothermal, with some of the water to drive the hydrothermal system possibly exsolved from either wet partial melt ascending from the APMB or from the wet APMB itself (Laumonier et al., 2017), an migrating through the region of elevated temperature depicted in Fig. 6. This assumption of a hydrothermal system is supported by observations of sulphur deposits, degassing, and surface thermal features, as described in Pritchard et al. (2018).

(5) Earthquake b-values > 1 for Region 2 (as defined in Fig. 4) suggest that much of this seismicity is also associated with fluids. Other mechanisms such as thermal stress gradients (Warren and Latham, 1970) and material heterogeneities (Mogi, 1962) are unlikely to cause high b-values as the deep crust is likely more homogeneous than the shallower crust discussed in (4). Given the spatial distribution of this seismicity, it is suggested that this is again fluids, perhaps from the subducting slab at depths of 100 to 150 km bsl (Cahill and Isacks, 1992; Prezzi et al., 2009), trapped and/or migrating along pre-existing faults, towards the APMB. This hypothesis is affirmed by the S-wave body-wave tomography results (Kukarina et al., 2017) shown in Fig. 7d, which show an anomalously low shear-velocity region extending from the slab towards the deep seismicity we observe. Seismicity above the slab that is used in the tomography study of Kukarina et al. (2017) (West of the region plotted in Fig. 7d) also alludes to fluid ascent along faults, although we could not access the data to investigate this further. A similar feature is apparent from a joint ambient noise and receiver function tomography (Ward et al., 2017), shown in Fig. 7e, which has greater depth sensitivity but poorer lateral sensitivity than the body-wave tomography in Fig. 7d. This low velocity zone continues upwards along the path of the seismicity towards the depth of the APMB. This is an exciting result, since this seismicity is likely evidence of the migration of water from the dehydrating subducting slab through the crust. If correct, this observation has implications for where and how melt in the APMB originates, as well as the melt chemistry.

(6) Finally, for fluids to reach the shallow volcanic system, and likely the surface, they would have to pass through the APMB and elevated temperature region, as shown by the blue arrows in Fig. 6. These fluids would travel aseismically here, due to insufficient strain rates to cause elastic failure within the hot, ductile crust. Such fluid migration, whereby water-rich andesitic melt and/or magmatic water travels from the APMB to the shallower partial melt column structure beneath Uturuncu, is suggested in Gottsmann et al. (2017).

#### 4.3. Wider implications

Our observation of seismicity associated with fluid migration throughout the crust (conclusions (4) to (6)) has wider geological and economic implications. We assume here that a substantial component of the fluid flux is slab-derived H2O (Laumonier et al., 2017). This ascent of water via percolation along faults would provide an additional route of fluid ascent to that of magma ascent, such as that postulated in Collins et al. (2020). This additional water ascent mechanism could have two critical implications. Firstly, it could enhance the water content of magma in the APMB and Uturuncu volcanic system. Indeed, Laumonier et al. (2017) show that the APMB has an unusually high water content (>8 wt.% H<sub>2</sub>O). This water content is important since H<sub>2</sub>O degassing drives crystallisation, which increases the melt viscosity, inhibiting the ascent of melt towards the surface. Therefore, if the fluid ascent pathway that we observe can transport sufficient water to shallower melt storage regions, then this mechanism could play a critical role for controlling arc volcanism and volcanic eruptions. The second implication of the fluid ascent pathways is that it could facilitate the transport of minerals from the slab to the shallow hydrothermal system (Manning, 2004). This mechanism could promote enhanced mineral deposition at sufficiently shallow depths for mining.

# 5. Conclusions

We present new analysis of seismicity at Uturuncu volcano from two seismic experiments in operation between 2009 and 2012. The seismicity delineates: shallow fault structures (<4 km bsl) directly beneath Uturuncu; deeper seismicity below the APMB (>22 km bsl), defining a lower depth limit of the APMB, with this seismicity primarily laterally offset to the NE of Uturuncu; a lack of seismicity constrains the location of the APMB; and a shallower region above the APMB and below Uturuncu that is absent of seismicity. The APMB therefore does not extend below ~24 km bsl, suggesting an underlying cooler, brittle crust. This new analysis also reconciles a discordance in the distribution of earthquake depths for the shallow seismicity directly beneath Uturuncu presented in previous studies. The shallow region absent of seismicity directly below Uturuncu is interpreted to be a region of elevated temperature, indicative of the presence of partial melt and/or the advective heat transport by migrating fluids.

Moment magnitudes are calculated for all the recorded seismicity. These moment magnitudes provide estimates of *b*-values that are greater than one, as expected for a hydrothermally active volcanic system. This is contrary to previous studies that used local magnitudes to calculate *b*-values, with these studies finding *b*-values less than one. This result, further evidenced by theoretical arguments, emphasises the importance of using absolute moment magnitude rather than an empirical local magnitude scale. Intriguingly, *b*-values are found to be greater than one in both the shallow region directly beneath Uturuncu, and the deeper seismicity below the APMB.

High b-values in the shallow region are interpreted to be caused by trapping and migration of fluids along pre-existing faults, likely comprising a hydrothermal system. High b-values for the deeper seismicity (25 to 50 km bsl) suggest ascent of fluids, whether that be melt and/or water, from greater depths along a fault zone NE of Uturuncu. This seismicity likely elucidates a pathway of fluids from the subducting slab towards the surface. These fluids likely migrate upwards along fault zones, presumably fed from the dehydrating slab, before travelling aseismically through the APMB and shallower elevated temperature region. They then feed shallow hydrothermal systems, where the fluids reduce the

effective pressure on shallow faults, triggering the observed shallow (<4 km bsl) seismicity. These pathways of fluid ascent may provide a critical control on the water-content of melt in the crust, and hence the risk of volcanic eruptions, as well as promoting the accumulation of shallow mineral deposits.

### **CRediT authorship contribution statement**

**Thomas S. Hudson:** Conceptualization, Data curation, Formal analysis, Investigation, Methodology, Software, Visualization, Writing – original draft. **J-Michael Kendall:** Conceptualization, Funding acquisition, Methodology, Resources, Supervision, Writing – review & editing. **Matthew E. Pritchard:** Conceptualization, Funding acquisition, Project administration, Supervision, Writing – review & editing. **Jonathan D. Blundy:** Writing – review & editing. **Joachim H. Gottsmann:** Writing – review & editing.

### **Declaration of competing interest**

The authors declare that they have no known competing financial interests or personal relationships that could have appeared to influence the work reported in this paper.

# Acknowledgements

We thank all the PLUTONS team for discussions relating to the interpretations that no doubt improved this manuscript. We especially thank Ying Liu for providing her seismic velocity model that was used to locate the seismicity in this study, as well as Patricia McQueen for providing additional datasets from previous studies for producing the literature comparison plots included in this study. We also thank T. Greenfield and three anonymous reviewers whose comments have certainly improved the manuscript. The seismic data analysed in this study is publicly available from IRIS. The earthquake detection algorithm used in this study, QuakeMigrate (Winder et al., 2021), is available open source. We have also made the software used to calculate moment magnitudes and b-values, SeisSrcMoment (Hudson, 2020), available open source. Some of the figures were produced using Generic Mapping Tools (GMT) (Wessel et al., 2019). Much of the seismic data analysis was performed using ObsPy (Beyreuther et al., 2010). This work, and TSH were funded by the NSFGEO-NERC grant NE/S008845/1. MEP was funded by National Science Foundation grant EAR-1757495. JDB thanks the Royal Society for financial support through a Research Professorship (RP\R1\201048). The seismic data collection funded by the National Science Foundation grants 0908281 and 0909254, and the UK Natural Environment Research Council grant NE/G01843X/1.

# Appendix A. Supplementary material

Supplementary material related to this article can be found online at https://doi.org/10.1016/j.epsl.2021.117268.

# References

Alvizuri, C., Tape, C., 2016. Full moment tensors for small events ( $M_w < 3$ ) at Uturuncu volcano, Bolivia. Geophys. J. Int. 6, 1761–1783. https://doi.org/10.1093/gji/ggw247.

Beyreuther, M., Barsch, R., Krischer, L., Megies, T., Behr, Y., Wassermann, J., 2010. ObsPy: a python toolbox for seismology. Seismol. Res. Lett. 81 (3), 530–533. https://doi.org/10.1785/gssrl.81.3.530.

Bridges, D., Gao, S., 2006. Spatial variation of seismic *b*-values beneath Makushin Volcano, Unalaska Island, Alaska. Earth Planet. Sci. Lett. 245 (1–2), 408–415. https://doi.org/10.1016/j.epsl.2006.03.010.

Brune, J.N., 1970. Tectonic stress and the spectra of seismic shear waves from earth-quakes. J. Geophys. Res. 75 (26), 4997–5009.

- Butcher, A., Luckett, R., Kendall, J.-M., Baptie, B., 2020. Seismic magnitudes, corner frequencies, and microseismicity: using ambient noise to correct for high-frequency attenuation. Bull. Seismol. Soc. Am. 110 (3), 1260–1275. https://doi.org/10.1785/0120190032.
- Cahill, T., Isacks, B.L., 1992. Seismicity and shape of the subducted Nazca Plate. J. Geophys. Res. 97 (B12). https://doi.org/10.1029/92jb00493.
- Cesca, S., 2020. Seiscloud, a tool for density-based seismicity clustering and visualization. J. Seismol. 24 (3), 443–457. https://doi.org/10.1007/s10950-020-09921-8
- Chmielowski, J., Zandt, G., Haberland, C., 1999. The central Andean Altiplano-Puna magma body. Geophys. Res. Lett. 26 (6), 783–786. https://doi.org/10.1029/1999GI.900078.
- Collins, W.J., Murphy, J.B., Johnson, T.E., Huang, H.Q., 2020. Critical role of water in the formation of continental crust. Nat. Geosci. 13 (5), 331–338. https://doi.org/ 10.1038/s41561-020-0573-6.
- Comeau, M.J., Unsworth, M.J., Cordell, D., 2016. New constraints on the magma distribution and composition beneath Volcán Uturuncu and the southern Bolivian Altiplano from magnetotelluric data. Geosphere 12 (5), 1391–1421. https://doi.org/10.1130/GES01277.1.
- Deichmann, N., 2017. Theoretical basis for the observed break in ML/MW scaling between small and large earthquakes. Bull. Seismol. Soc. Am. 107 (2), 505–520. https://doi.org/10.1785/0120160318.
- Del Potro, R., Díez, M., Blundy, J., Camacho, A.G., Gottsmann, J., 2013. Diapiric ascent of silicic magma beneath the Bolivian Altiplano. Geophys. Res. Lett. 40 (10), 2044–2048. https://doi.org/10.1002/grl.50493.
- Drew, J., White, R.S., Tilmann, F., Tarasewicz, J., 2013. Coalescence microseismic mapping. Geophys. J. Int. 195 (3), 1773–1785. https://doi.org/10.1093/gji/ggt331.
- El-Isa, Z.H., Eaton, D.W., 2014. Spatiotemporal variations in the *b*-value of earth-quake magnitude-frequency distributions: classification and causes. Tectonophysics 615–616, 1–11. https://doi.org/10.1016/j.tecto.2013.12.001.
- Ester, M., Kriegel, H.-P., Sander, J., Xu, X., 1996. A density-based algorithm for discovering clusters in large spatial databases with noise. In: KDD-96 Proceedings. Elsevier, pp. 226–231. Retrieved from https://linkinghub.elsevier.com/retrieve/pii/B9780444527011000673.
- Farrell, J., Husen, S., Smith, R.B., 2009. Earthquake swarm and *b*-value characterization of the Yellowstone volcano-tectonic system. J. Volcanol. Geotherm. Res. 188 (1–3), 260–276. https://doi.org/10.1016/j.jvolgeores.2009.08.008.
- Gottsmann, J., Blundy, J., Henderson, S., Pritchard, M.E., Sparks, R.S.J., 2017. Thermomechanical modeling of the Altiplano-Puna deformation anomaly: multiparameter insights into magma mush reorganization. Geosphere 13 (4), 1042–1045. https://doi.org/10.1130/GES01420.1.
- Gottsmann, Joachim, del Potro, R., Muller, C., 2018. 50 years of steady ground deformation in the Altiplano-Puna region of southern Bolivia. Geosphere 14 (1), 65–73. https://doi.org/10.1130/GES01570.1.
- Greenfield, T., White, R.S., 2015. Building Icelandic igneous crust by repeated melt injections. J. Geophys. Res., Solid Earth 120 (11), 7771–7788. https://doi.org/10.1002/2015/B012009.
- Greenfield, T., White, R.S., Winder, T., Ágústsdóttir, T., 2018. Seismicity of the Askja and Bárðarbunga volcanic systems of Iceland, 2009–2015. J. Volcanol. Geotherm. Res. https://doi.org/10.1016/j.jvolgeores.2018.08.010.
- Greenfield, T., White, R.S., Winder, T., Ágústsdóttir, T., 2020. Seismicity of the Askja and Bardarbunga volcanic systems of Iceland, 2009–2015. J. Volcanol. Geotherm. Res. 391. https://doi.org/10.1016/j.jvolgeores.2018.08.010.
- Hanks, T.C., Kanamori, H., 1979. A moment magnitude scale. J. Geophys. Res. 84 (B5), 2348. https://doi.org/10.1029/JB084iB05p02348.
- Henderson, S.T., Pritchard, M.E., 2017. Time-dependent deformation of Uturuncu volcano, Bolivia, constrained by GPS and InSAR measurements and implications for source models. Geosphere 13 (6), 1834–1854. https://doi.org/10.1130/GES01203.
- Hudson, T.S., 2020. TomSHudson/SeisSrcMoment: First formal release (Version 1.0.0). Zenodo. https://doi.org/10.5281/zenodo.4010325.
- Hudson, T.S., White, R.S., Greenfield, T., Ágústsdóttir, T., Brisbourne, A., Green, R.G., 2017. Deep crustal melt plumbing of Bárðarbunga volcano, Iceland. Geophys. Res. Lett. 44 (17), 8785–8794. https://doi.org/10.1002/2017GL074749.
- Hudson, T.S., Smith, J., Brisbourne, A., White, R., 2019. Automated detection of basal icequakes and discrimination from surface crevassing. Ann. Glaciol. 60 (79), 1–11. https://doi.org/10.1017/aog.2019.18.
- Hutchinson, L., 2015. Double-Difference Relocation of Earthquakes at Uturuncu Volcano, Bolivia, and Interior Alaska. MS Thesis. University of Alaska, Fairbanks.
- Illsley-Kemp, F., Keir, D., Bull, J.M., Ayele, A., Hammond, J.O.S., Kendall, J.M., et al., 2017. Local earthquake magnitude scale and b-value for the Danakil region of northern afar. Bull. Seismol. Soc. Am. 107 (2), 521–531. https://doi.org/10.1785/ 0120150253.
- Jay, J.A., Pritchard, M.E., West, M.E., Christensen, D., Haney, M., Minaya, E., et al., 2012. Shallow seismicity, triggered seismicity, and ambient noise tomography at the long-dormant Uturuncu Volcano, Bolivia. Bull. Volcanol. 74 (4), 817–837. https://doi.org/10.1007/s00445-011-0568-7.
- Kukarina, E., West, M., Keyson, L.H., Koulakov, I., Tsibizov, L., Smirnov, S., 2017. Focused magmatism beneath Uturuncu volcano, Bolivia: insights from seismic tomography and deformation modeling. Geosphere 13 (6), 1855–1866. https://doi.org/10.1130/GES01403.1.

- Laumonier, M., Gaillard, F., Muir, D., Blundy, J., Unsworth, M., 2017. Giant magmatic water reservoirs at mid-crustal depth inferred from electrical conductivity and the growth of the continental crust. Earth Planet. Sci. Lett. 457, 173–180. https://doi.org/10.1016/j.epsl.2016.10.023.
- Lavayssière, A., Greenfield, T., Keir, D., Ayele, A., Kendall, J.M., 2019. Local seismicity near the actively deforming Corbetti volcano in the Main Ethiopian Rift. J. Volcanol. Geotherm. Res. 381, 227–237. https://doi.org/10.1016/j.jvolgeores.2019.06.
- Leidig, M., Zandt, G., 2003. Modeling of highly anisotropic crust and application to the Altiplano-Puna volcanic complex of the central Andes. J. Geophys. Res., Solid Earth 108 (B1). https://doi.org/10.1029/2001jb000649, ESE 5-1-ESE 5-15.
- Lomax, A., Virieux, J., 2000. Probabilistic earthquake location in 3D and layered models. In: Advances in Seismic Event Location, Volume 18 of the Series Modern Approaches in Geophysics, pp. 101–134.
- Maher, S., Kendall, J., 2018. Crustal anisotropy and state of stress at Uturuncu Volcano, Bolivia, from shear-wave splitting measurements and magnitude frequency distributions in seismicity. Earth Planet. Sci. Lett. 495, 38–49. https://doi.org/10.1016/j.epsl.2018.04.060.
- Manning, C.E., 2004. The chemistry of subduction-zone fluids. Earth Planet. Sci. Lett. 223 (1–2), 1–16. https://doi.org/10.1016/j.epsl.2004.04.030.
- Mogi, K., 1962. Study of elastic shocks caused by the fracture of heterogeneous materials and its relations to earthquake phenomena. Bull. Earthq. Res. Inst.
- Muir, D.D., Barfod, D.N., Blundy, J.D., Rust, A.C., Sparks, R.S.J., Clarke, K.M., 2015. The temporal record of magmatism at Cerro Uturuncu, Bolivian Altiplano. Geol. Soc. Spec. Publ. 422 (1), 57–83. https://doi.org/10.1144/SP422.1.
- Murru, M., Console, R., Falcone, G., Montuori, C., Sgroi, T., 2007. Spatial mapping of the *b* value at Mount Etna, Italy, using earthquake data recorded from 1999 to 2005. J. Geophys. Res., Solid Earth 112 (12), 1–15. https://doi.org/10.1029/2006[B004791.
- Pearson, K., 1901. On lines and planes of closest fit to systems of points in space. Lond. Edinb. Dublin Philos. Mag. J. Sci. 2 (11), 559–572. https://doi.org/10.1080/14786440109462720.
- Power, J.A., Wyss, M., Latchman, J.L., 1998. Spatial variations in the frequency-magnitude distribution. Geophys. Res. Lett. 25 (19), 3653–3656.
- Prezzi, C.B., Götze, H.J., Schmidt, S., 2009. 3D density model of the Central Andes. Phys. Earth Planet. Inter. 177 (3–4), 217–234. https://doi.org/10.1016/j.pepi. 2009.09.004.
- Pritchard, M.E., de Silva, S.L., Michelfelder, G., Zandt, G., McNutt, S.R., Gottsmann, J., et al., 2018. Synthesis: PLUTONS: investigating the relationship between pluton growth and volcanism in the Central Andes. Geosphere 14 (3), 954–982. https://doi.org/10.1130/GES01578.1.
- Roberts, N.S., Bell, A.F., Main, I.G., 2015. Are volcanic seismic b-values high, and if so when? J. Volcanol. Geotherm. Res. 308, 127–141. https://doi.org/10.1016/j. ivolgeores.2015.10.021.
- Roberts, N.S., Bell, A.F., Main, I.G., 2016. Mode switching in volcanic seismicity: El Hierro 2011–2013. Geophys. Res. Lett. 43 (9), 4288–4296. https://doi.org/10.1002/2016GL068809.
- Rubin, A.M., 1993. Dikes vs. diapirs in viscoelastic rock. Earth Planet. Sci. Lett. 117 (3–4), 653–670. https://doi.org/10.1016/0012-821X(93)90109-M.
- Schlaphorst, D., Kendall, J.M., Collier, J.S., Verdon, J.P., Blundy, J., Baptie, B., et al., 2016. Water, oceanic fracture zones and the lubrication of subducting plate boundaries-insights from seismicity. Geophys. J. Int. 204 (3), 1405–1420. https://doi.org/10.1093/gji/ggv509.
- Schmitz, M., Heinsohn, W.D., Schilling, F.R., 1997. Seismic, gravity and petrological evidence for partial melt beneath the thickened Central Andean crust (21–23°S). Tectonophysics 270 (3–4), 313–326. https://doi.org/10.1016/S0040-1951(96)00217-X.
- Shelly, D.R., Hill, D.P., 2011. Migrating swarms of brittle-failure earthquakes in the lower crust beneath Mammoth Mountain, California. Geophys. Res. Lett. 38 (20), 1–6. https://doi.org/10.1029/2011GL049336.
- Smith, J.D., White, R.S., Avouac, J.-P., Bourne, S., 2020. Probabilistic earthquake locations of induced seismicity in the Groningen region, the Netherlands. Geophys. J. Int. 222 (1), 507-516. https://doi.org/10.1093/gji/ggaa179.
- Sparks, R.S.J., Folkes, C.B., Humphreys, M.C.S., Barfod, D.N., Clavero, J., Sunagua, M.C., et al., 2008. Uturuncu volcano, Bolivia: volcanic unrest due to mid-crustal magma intrusion. Am. J. Sci. 308 (6), 727–769. https://doi.org/10.2475/06.2008.
- Stork, A.L., Verdon, J.P., Kendall, J.M., 2014. The robustness of seismic moment and magnitudes estimated using spectral analysis. Geophys. Prospect. 62 (4), 862–878. https://doi.org/10.1111/1365-2478.12134.
- Ward, K.M., Porter, R.C., Zandt, G., Beck, S.L., Wagner, L.S., Minaya, E., Tavera, H., 2013. Ambient noise tomography across the Central Andes. Geophys. J. Int. 194 (3), 1559–1573. https://doi.org/10.1093/gji/ggt166.
- Ward, K.M., Zandt, G., Beck, S.L., Christensen, D.H., McFarlin, H., 2014. Seismic imaging of the magmatic underpinnings beneath the Altiplano-Puna volcanic complex from the joint inversion of surface wave dispersion and receiver functions. Earth Planet. Sci. Lett. 404, 43–53. https://doi.org/10.1016/j.epsl.2014.07.022.
- Ward, K.M., Delph, J.R., Zandt, G., Beck, S.L., Ducea, M.N., 2017. Magmatic evolution of a Cordilleran flare-up and its role in the creation of silicic crust. Sci. Rep. 7 (1), 1-8. https://doi.org/10.1038/s41598-017-09015-5.

- Warren, N.W., Latham, G.V., 1970. Experimental study of thermally induced microfracturing and its relation to volcanic seismicity. J. Geophys. Res. 75 (23), 4455–4464. https://doi.org/10.1029/jb075i023p04455.
- Wessel, P., Luis, J.F., Uieda, L., Scharroo, R., Wobbe, F., Smith, W.H.F., Tian, D., 2019. The generic mapping tools version 6. Geochem. Geophys. Geosyst. 20 (11), 5556–5564. https://doi.org/10.1029/2019GC008515.
- Wiemer, S., McNutt, S.R., Wyss, M., 1998. Temporal and three-dimensional spatial analyses of the frequency-magnitude distribution near Long Valley Caldera, California. Geophys. J. Int. 134 (2), 409–421. https://doi.org/10.1046/j.1365-246X. 1998.00561.x.
- Wilks, M., Kendall, J.M., Nowacki, A., Biggs, J., Wookey, J., Birhanu, Y., et al., 2017. Seismicity associated with magmatism, faulting and hydrothermal circulation at Aluto Volcano, Main Ethiopian Rift. J. Volcanol. Geotherm. Res. 340, 52–67. https://doi.org/10.1016/j.jvolgeores.2017.04.003.
- Winder, T., Bacon, C., Smith, J.D., Hudson, T.S., Drew, J., White, R.S., 2021. QuakeMigrate v1.0.0. Zenodo. https://doi.org/10.5281/zenodo.4442749.
- Zandt, G., Leidig, M., Chmielowski, J., Baumont, D., Yuan, X., 2003. Seismic detection and characterization of the Altiplano-Puna magma body, Central Andes. Pure Appl. Geophys. 160 (3–4), 789–807. https://doi.org/10.1007/PL00012557.